

Non-collinear Magnetic Order in the Double Perovskites: Double Exchange on a Geometrically Frustrated Lattice

Rajarshi Tiwari and Pinaki Majumdar
Harish-Chandra Research Institute,
Chhatnag Road, Jhusi, Allahabad 211019, India
 (Dated: 30 April 2011)

Double perovskites of the form $A_2BB'O_6$ usually involve a transition metal ion, B, with a large magnetic moment, and a non magnetic ion B' . While many double perovskites are ferromagnetic, studies on the underlying model reveal the possibility of antiferromagnetic phases as well *driven by electron delocalisation*. In this paper we present a comprehensive study of the magnetic ground state and T_c scales of the minimal double perovskite model in three dimensions using a combination of spin-fermion Monte Carlo and variational calculations. In contrast to two dimensions, where the effective magnetic lattice is bipartite, three dimensions involves a geometrically frustrated face centered cubic (FCC) lattice. This promotes non-collinear spiral states and ‘flux’ like phases in addition to collinear anti-ferromagnetic order. We map out the possible magnetic phases for varying electron density, ‘level separation’ $\epsilon_B - \epsilon_{B'}$, and the crucial $B'B'$ (next neighbour) hopping t' .

Keywords: double perovskite, double exchange, geometric frustration, non-collinear magnetism

I. INTRODUCTION

Double perovskites (DP) constitute a large family of materials¹ with molecular formula $A_2BB'O_6$, where A is an alkali or alkaline earth metal, and B and B' are typically transition metals. Although double perovskites have been studied for decades², the discovery of high T_c ferromagnetism and half-metallicity in Sr_2FeMoO_6 has led to renewed interest in their properties. Later, in a number of explorations it was discovered that these materials are candidates for various technological applications, *e.g.*, in spintronics³ (Sr_2FeMoO_6), magneto-dielectrics^{4,5} (La_2NiMnO_6), and magneto-optics⁶ (Sr_2CrOsO_6, Sr_2CrReO_6). Their properties are determined by the couplings on the B and B' ions, the B and B' valence state, and the structural order in the B- B' lattice.

The magnetism in the DP’s arises from a combination of (i) Hund’s coupling on the B, B' ions and (ii) electron delocalisation. While there are important DP’s where both B and B' are magnetic ions, in the current work we will restrict ourselves to materials where only one ion, B, say, is magnetic. For example, in Sr_2FeMoO_6 (SFMO) the B atom (Fe) is magnetic while B' (Mo) is non magnetic⁷. Even in this restricted class, a large variety of compounds can be realized by taking $3d$, $4d$ or $5d$ transition metals as B and B' , and alkaline earths or rare-earths as A. These lead to a variety of properties, *e.g.*, high T_c ferro(or ferri) magnetism (FM), with half-metallic^{8,9} or insulating¹⁰ behaviour.

There have been several attempts at a theoretical understanding of the magnetism in these materials. These consist of (i) *ab initio* electronic structure calculations, and (ii) model Hamiltonian based approaches. The *ab initio* calculations⁵⁻⁷ provide material specific information about the electronic structure and allow a rough estimate¹¹ of the T_c . Unfortunately, these calculations are rather complicated for non-collinear magnetic phases

that are likely in a frustrated magnetic lattice, see Fig.1. In such situations model Hamiltonian studies can provide some insight on possible ordered states.

Early model calculations for DP’s used dynamical mean field theory (DMFT) to estimate T_c and the magnetic stability window^{12,13}, focusing on ferromagnetism. Earlier work on the classical Kondo lattice¹⁴⁻¹⁷ had revealed that variation in carrier density can lead to a wide variety of phases in a spin-fermion problem. Indeed, calculation¹⁸ in a two dimensional (2D) model of DP’s confirmed the existence of antiferromagnetic (AF), albeit collinear, phases. The ‘frustrated’ character of the three dimensional (3D) DP lattice raises the intriguing possibility of doping driven non collinear magnetic phases as well. Our study aims to explore this issue in detail.

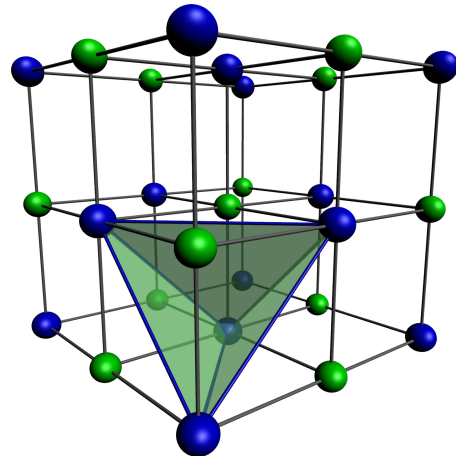


FIG. 1: Colour online: The structure of B- B' lattice in a ordered double perovskite. The B and B' alternate (as in rock-salt) in the ordered structure. If the bottom corner (blue) atom is B, then its B nearest neighbours (connected by lines) are also nearest neighbours of each other. The triangles preclude a ‘G type’ antiferromagnetic phase.

Our main results are the following. Using a combination of Monte Carlo and variational minimization, we map out the magnetic ground state (Fig.2) at large Hund's coupling for varying electron density and B-B' level separation. In addition to FM, and collinear A and C type order, the phase diagram includes large regions of non-collinear 'flux' and spiral phases and windows of phase separation. Modest B'B' hopping leads to significant shift in the phase boundaries, and "particle-hole asymmetry". We provide estimates of the T_c of these non trivial magnetic phases.

The paper is organized as follows. In Section II we describe the model and methods, Section III describes our results in the particle-hole symmetric case ($t' = 0$), and Section IV describes the effect of finite t' . Section V discusses some issues of modeling the real DP. Section VI concludes the paper.

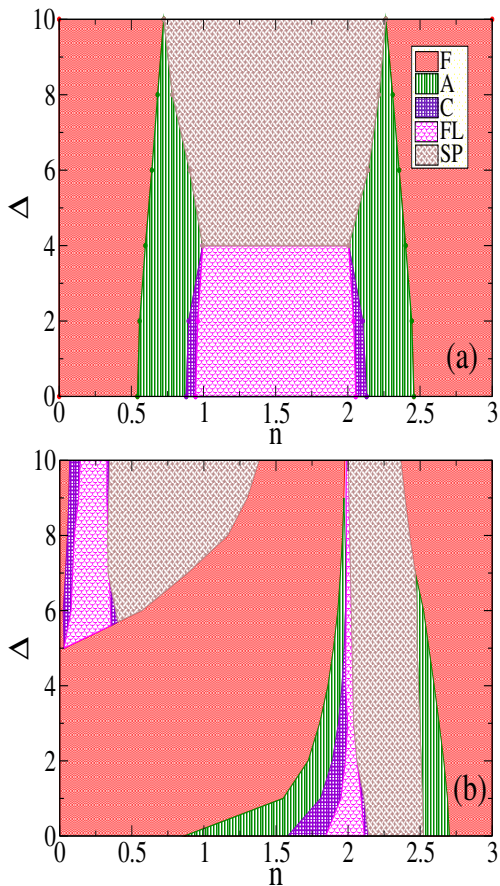


FIG. 2: Colour online: Magnetic ground state for varying electron density, n , and effective B-B' level separation, Δ . Top: phase diagram with only BB', *i.e.*, nearest neighbour, hopping. Bottom: phase diagram when an additional B'B' hopping, $t'/t = -0.3$, is included. The labels are: F (ferromagnet), A (planar phase), C (line like), FL ('flux') and SP (spiral). This figure does not show the narrow windows of phase separation in the model. The phase diagrams are generated via a combination of Monte Carlo and variational calculations on lattices of size upto $20 \times 20 \times 20$.

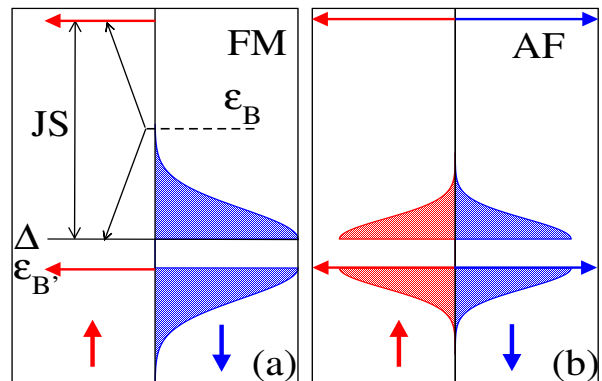


FIG. 3: Colour online: Level scheme and schematic band structure for the DP model when only B-B' hopping is allowed. The arrows denote localised atomic levels. Red and blue denote \uparrow and \downarrow spins respectively. The atomic level scheme is shown in (a), where the spin degenerate B' levels are at $\epsilon_{B'} = 0$ and the spin split B levels are at $\epsilon_B \pm JS/2$. We define the effective B level as $\Delta = \epsilon_B - JS/2$. When $JS \gg t$, the levels at $\epsilon_{B'}$ and Δ hybridise to create bands, shown for the FM case in (a), and for a collinear AF phase in (b).

II. MODEL AND METHOD

Previous study of double perovskites in two dimensions²⁰ revealed three collinear phases, namely FM, a diagonal stripe phase (FM lines coupled antiferromagnetically) and a 'G type' phase (up spin surrounded by down and *vice versa*). In 2D the B sub-lattice is square and bipartite, so there is no frustration. In a 3D *simple cubic* B lattice the counterparts of the 2D phases would be FM, A type (planar), C type (line like) and G type. The magnetic B ion lattice in the DP's is, however, FCC which is *non-bipartite*, so while one can construct FM and planar A type phases, the C type phase is modified and the G type phase cannot exist.

Fig.1 briefly indicates why it is impossible to have an 'up'(\uparrow) B ion to be surrounded by only 'down'(\downarrow) B ions, *i.e.*, the G type arrangement. Two B neighbours of a B ion are also neighbours of each other, frustrating G type order. The suppression of the G type phase, which occupies a wide window in 2D, requires us to move beyond collinear phases in constructing the 3D phase diagram. We will discuss the variational family in Section II C.

A. Model

The alternating arrangement of B and B' ions in the ordered cubic double perovskites is shown in Fig.1. We use the following one band model on that structure:

$$H = \epsilon_B \sum_{i \in B} f_{i\sigma}^\dagger f_{i\sigma} + \epsilon_{B'} \sum_{i \in B'} m_{i\sigma}^\dagger m_{i\sigma} - \mu \hat{N} - t \sum_{\langle ij \rangle} f_{i\sigma}^\dagger m_{j\sigma} + J \sum_{i \in B} \mathbf{S}_i \cdot f_{i\alpha}^\dagger \vec{\sigma}_{\alpha\beta} f_{i\beta}$$

The f^\dagger correspond to the B ions and the m^\dagger to the B'. ϵ_B and $\epsilon_{B'}$ are ‘onsite’ energy on the B and B' sites respectively, e.g., the t_{2g} level energy of Fe and Mo in SFMO. μ is the chemical potential and $\hat{N} = \sum_{i\sigma} (f_{i\sigma}^\dagger f_{i\sigma} + m_{i\sigma}^\dagger m_{i\sigma})$ is the total electron number operator. t is the hopping amplitude between nearest neighbour B and B' ions. We augment this model later to study first neighbour B'B' hopping t' as well. J is the (Hund's) coupling between the B core spin and the f conduction electron. We will use $|\mathbf{S}_i| = 1$, and absorb the magnitude of \mathbf{S} in J . $\sigma_{\alpha\beta}^\mu$ are the Pauli matrices.

The model has parameters J , ϵ_B , $\epsilon_{B'}$, and μ (or n). Since only the level difference matters, we set $\epsilon_{B'} = 0$. We have set $t = 1$, and use $J/t \gg 1$ so that the conduction electron spin at the B site is slaved to the core spin orientation. However, to keep the *effective* level difference between B and B' sites finite we use the parameter $\Delta = \epsilon_B - J/2$, and explore the phases as a function of n and Δ/t . We will present results for $t'/t = 0$ and ± 0.3 .

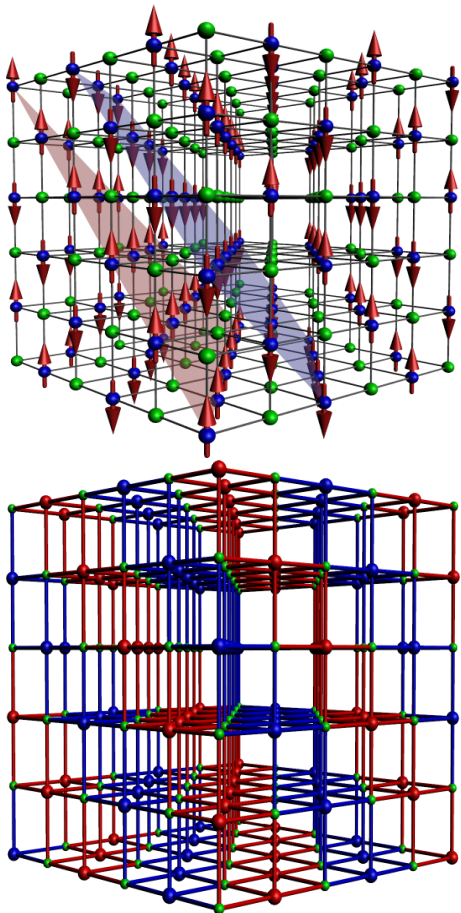


FIG. 4: Colour online. Top: Spin configuration for ‘A type’ order. The spins are parallel within the 111 planes (shown) and are antiparallel between neighbouring planes. Bottom: The differently coloured bonds show the electron delocalisation pathway for up and down spin electrons in the A type phase. The delocalisation is effectively two dimensional.

A schematic for the levels is shown in Fig.3. The structural unit cell of the system has 2 (one B, one B') atoms, which amounts to 4 atomic levels (2 up spin, 2 down spin). The two spin levels at the B site are separated by JS and overlap with 2 spin degenerate levels of the B' site at $\epsilon_{B'} = 0$. We take the large J limit, and take $\epsilon_B = J/2 + \Delta$ with Δ in the range (0-10). One B band become centered at Δ and second goes to $JS + \Delta$. In this situation the down spin B and two B' bands overlap while up spin B band is always empty. The relevant electron density window includes the lowest three bands, so our electron density will be in the range $[0, 3]$.

To get a general feel of the band structure of the particle hole symmetric case, we notice that we have three levels (excluding the highest f_\uparrow level at $JS + \Delta$ which remains empty and is redundant for our purpose) in atomic limit. These include one spin slaved f_\downarrow level at Δ , and the two m_\uparrow , m_\downarrow , levels which overlap with the f_\downarrow levels depending on the spin configurations. This overlap leads to electron delocalisation and band formation.

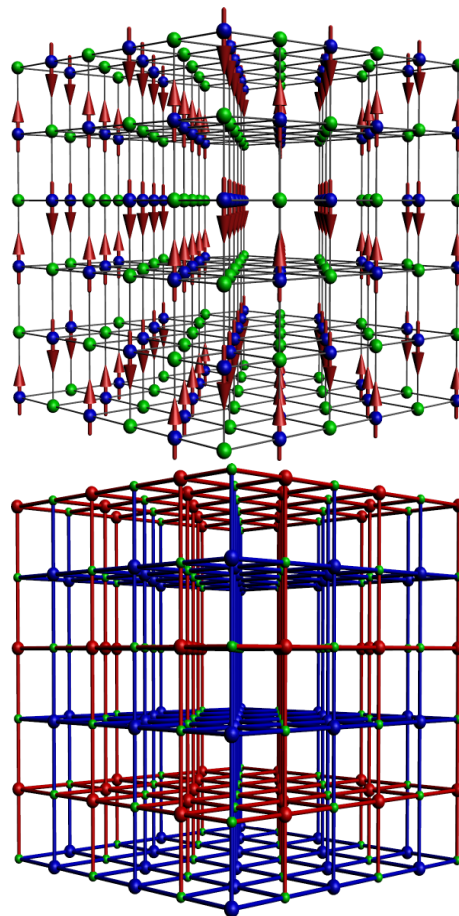


FIG. 5: Colour online. Top: Spin configuration in the ‘C type’ phase. Core spins are parallel on alternating 110 planes, and antiparallel on neighbouring planes. Bottom: the delocalisation path, consisting of the 110 planes and the horizontal 001 planes.

For the FM, Fig.3.(a), only one spin channel (say m_\downarrow) gets to delocalise through f sites and forms two bands, separated by a band gap of Δ , while other spin channel (say m_\uparrow) is localised at 0.

For collinear AF configurations, Fig.3.(b), the conduction path gets divided into two sub-lattices, such that each spin channel gets to delocalise in one sub-lattice (in which all the core spins point in same direction, making the sub-lattice ferromagnetic.) See Fig.4, and Fig.5 for the details of the conduction path. In one such sub-lattice, only one of the \uparrow or \downarrow delocalised, the other remains localised. The roles of \uparrow and \downarrow are reversed in going from one sub-lattice to other, as a result one gets spin-degenerate localised and dispersive bands for AF phases.

B. Monte Carlo method

The model involves spins and fermions, and if the spins are ‘large’, $2S \gg 1$, they can be approximated as classical. This should be reasonable in materials like SFMO

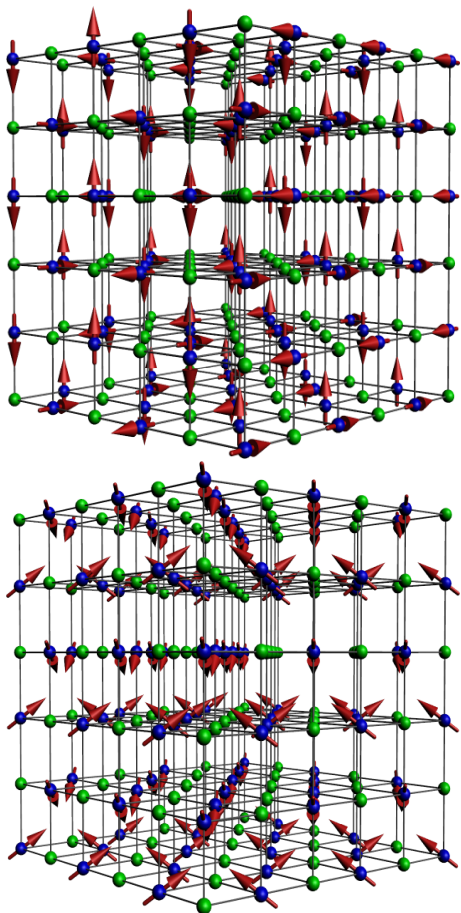


FIG. 6: Colour online. Spin configuration for a typical spiral phase (top) and the ‘flux’ phase (bottom). Since the spin configurations are non-collinear the electrons delocalise over the whole system.

where $S = 5/2$. Even in the classical limit these spins are annealed variables and their ground state or thermal fluctuations have to be accessed via iterative diagonalisation of the electronic Hamiltonian. We use a ‘traveling cluster’ Monte Carlo (MC) method where the cost of a spin update is estimated via a small cluster Hamiltonian instead of diagonalising the whole system¹⁹.

We typically use a $12 \times 12 \times 12$ system with the energy cost of a move estimated via a 4^3 cluster built around the reference site. We principally track the magnetic structure factor

$$S(\mathbf{q}) = \frac{1}{N^2} \sum_{\mathbf{r}, \mathbf{r}'} \langle \mathbf{S}_{\mathbf{r}} \cdot \mathbf{S}_{\mathbf{r}'} \rangle e^{i\mathbf{q} \cdot (\mathbf{r} - \mathbf{r}')}$$

where $\langle \dots \rangle$ denote thermal average.

Although the magnetic lattice is FCC, the electrons delocalise on the combined B-B’ system which is a cubic lattice. Hence we define our wave-numbers \mathbf{q} with respect to the full B-B’ lattice. As a result even a simple state like the ferromagnet corresponds to peaks at $\mathbf{q} = (0, 0, 0)$ and $\mathbf{q} = (\pi, \pi, \pi)$ and not just $\mathbf{q} = (0, 0, 0)$. This is because the spin field is also defined on B’ sites and it has to have zeros on these sites.

This complication, and the possibility of spiral phases, *etc*, mean that (i) there are multiple \mathbf{q} values which could be significant at low temperature, and (ii) the $S(\mathbf{q})$ peaks could be small even in the ordered state. Combined with the intrinsic noise in MC data (which is enhanced due to a complex energy landscape, discussed later) it is sometimes difficult to identify complicated ordered phases. Therefore, to complement the MC results we have also used the following variational scheme.

C. Variational scheme

We explore a set of magnetic states, comparing their energy to locate the minimum within that family for a fixed set of electronic parameters. We use:

$$\mathbf{S}_{\mathbf{r}} = p(\mathbf{r}) \{ \hat{x} \sin \theta(\mathbf{r}) \cos \phi(\mathbf{r}) + \hat{y} \sin \theta(\mathbf{r}) \sin \phi(\mathbf{r}) + \hat{z} \cos \theta(\mathbf{r}) \}$$

where $\theta(\mathbf{r}) = \mathbf{q}_\theta \cdot \mathbf{r}$ and $\phi(\mathbf{r}) = \mathbf{q}_\phi \cdot \mathbf{r}$ with $p(\mathbf{r}) = 1$ if $\mathbf{r} \in B$ and $p(\mathbf{r}) = 0$ if $\mathbf{r} \in B'$. \hat{x} , *etc.*, are unit vectors in the corresponding directions.

The vector field $\mathbf{S}_{\mathbf{r}}$ is characterized by the two wave-vectors \mathbf{q}_θ and \mathbf{q}_ϕ . For a periodic configuration, these should be $\mathbf{q}_\theta = \frac{2\pi}{L}(q_1, q_2, q_3)$ and $\mathbf{q}_\phi = \frac{2\pi}{L}(p_1, p_2, p_3)$, where q_i ’s and p_i ’s are integers, each of which take L values in $\{0, 1, 2, 3, \dots, L-1\}$. There are $\sim L^6$ ordered magnetic configurations possible, within this family, on a simple cubic lattice of linear dimension L .

The use of symmetries, *e.g.*, permuting components of \mathbf{q}_θ , *etc.*, reduces the number of candidates somewhat, but they still scale as $\sim L^6$. For a general combination of $\mathbf{q}_\theta, \mathbf{q}_\phi$ the eigenvalues of H cannot be analytically obtained because of the non trivial mixing of electronic

Phase	Peak location in $S(\mathbf{q})$
Ferromagnet (FM)	$(0,0,0),(\pi,\pi,\pi)$
A-type antiferromagnet (A)	$(\frac{\pi}{2},\frac{\pi}{2},\frac{\pi}{2}),(\frac{3\pi}{2},\frac{3\pi}{2},\frac{3\pi}{2})$
C-type antiferromagnet (C)	$(0,0,\pi),(\pi,\pi,0)$
'flux' (FL)	$(\pi,0,0), (0,\pi,0), (0,0,\pi), (\pi,\pi,0), (\pi,0,\pi), (0,\pi,\pi)$
$\uparrow\uparrow\downarrow$ phase	$(\frac{\pi}{2},0,0), (\frac{3\pi}{2},0,0), (\frac{\pi}{2},\pi,\pi), (\frac{3\pi}{2},\pi,\pi)$
\mathbf{SP}_1 ($\mathbf{q}_\theta, \mathbf{q}_\phi$) = $(0, \frac{\pi}{2}, \pi), (0, 0, 0)$	$(0, \frac{\pi}{2}, \pi), (\pi, \frac{\pi}{2}, 0), (0, \frac{3\pi}{2}, \pi), (\pi, \frac{3\pi}{2}, 0)$
\mathbf{SP}_2 ($\mathbf{q}_\theta, \mathbf{q}_\phi$) = $(0, \frac{\pi}{2}, \pi), (0, \frac{\pi}{2}, 0)$	$(0, \frac{\pi}{2}, \pi), (\pi, \frac{\pi}{2}, 0), (0, \frac{3\pi}{2}, \pi), (\pi, \frac{3\pi}{2}, 0)$ $(0, 0, \pi), (\pi, 0, 0) + (\pi, \pi, 0) + (0, \pi, \pi)$
\mathbf{SP}_3 ($\mathbf{q}_\theta, \mathbf{q}_\phi$) = $(0, \frac{\pi}{2}, \pi), (\frac{\pi}{2}, 0, \frac{\pi}{2})$	$(0, \frac{\pi}{2}, \pi), (\pi, \frac{\pi}{2}, 0), (0, \frac{3\pi}{2}, \pi), (\pi, \frac{3\pi}{2}, 0)$ $(\frac{\pi}{2}, \frac{\pi}{2}, \frac{3\pi}{2}), (\frac{3\pi}{2}, \frac{3\pi}{2}, \frac{\pi}{2}), (\frac{\pi}{2}, \frac{3\pi}{2}, \frac{3\pi}{2}), (\frac{3\pi}{2}, \frac{\pi}{2}, \frac{\pi}{2})$

TABLE I: Candidate phases, the associated $\mathbf{q}_\theta, \mathbf{q}_\phi$, for the spirals, and the peak locations in the structure factor $S(\mathbf{q})$. All the \mathbf{q} components have the same saturation value, given by $\frac{1}{2N_p}$, where N_p is the number of non-zero \mathbf{q} peaks in the $S(\mathbf{q})$. $N_p = 2$ for FM, A and C, $N_p = 4$ for $\uparrow\uparrow\downarrow$ and \mathbf{SP}_1 , $N_p = 6$ for flux and $N_p = 8$ for \mathbf{SP}_2 and \mathbf{SP}_3 . The factor of $\frac{1}{2}$ comes as we have half the spins at zero value, which halves the normalization.

momentum states. We have to resort to a real space diagonalisation. The Hamiltonian matrix size is $2N$ ($= 2L^3$) and the diagonalization cost is $\sim N^3$. So, a comparison of energies based on real space diagonalisation costs $\sim N^5$, possible only for $L \leq 8$.

We have adopted two strategies: (i) we have pushed this ' $\mathbf{q}_\theta, \mathbf{q}_\phi$ ' scheme to large sizes via a selection scheme described below, and (ii) for a few collinear configurations, where Fourier transformation leads to a small matrix, we have compared energies on sizes $\sim 400^3$.

First, scheme (i). For $L = 8$ we compare the energies of all possible phases, to locate the optimal pair $\{\mathbf{q}_\theta, \mathbf{q}_\phi\}_{min}$ for each μ . We then consider a larger system with a set of states in the neighbourhood of $\{\mathbf{q}_\theta, \mathbf{q}_\phi\}_{min}$. If we consider $\pm\pi/L$ variation about each component of $\mathbf{q}_{\theta,min}$, etc, that involves 3^6 states. The shortcoming of this method is that it explores only a restricted neighbourhood, dictated by the small size result. We have used $L = 12, 16, 20$ within this scheme.

The phases that emerge as a result of the above process are (i) Ferromagnet (FM), (ii) A-type, (iii) C-type, (iv) 'flux', and (v) three spirals $\mathbf{SP}_1, \mathbf{SP}_2, \mathbf{SP}_3$. A-type is consists of $(1, 1, 1)$ FM planes with alternate planes having opposite spin orientation (see Fig.4 top panel). If we convert each of these planes to alternating FM lines, so that the overall spin texture is alternating FM lines in all directions, we get C-type phase (see Fig.5).

The 'flux' phase is different from the spiral families described using period vectors $\mathbf{q}_\theta, \mathbf{q}_\phi$. It is the augmented version of 'flux' phase used in cubic lattice double exchange model by Alonso *et al*¹⁶(Table-I). It has spin-ice like structure, and is described by

$$\mathbf{S}(\mathbf{r}) = \frac{p(\mathbf{r})}{\sqrt{3}}((-1)^{y+z}, (-1)^{z+x}, (-1)^{x+y})$$

The spiral \mathbf{SP}_n phases are characterised by comensurate values of $\mathbf{q}_\theta, \mathbf{q}_\phi$ (See Table I for details of periods and the $S(\mathbf{q})$ peaks).

The simplest, \mathbf{SP}_1 can be viewed as $\frac{\pi}{2}$ -angle pitch in the $(110), (101)$ and (011) directions. The other two spirals $\mathbf{SP}_2, \mathbf{SP}_3$ are respectively C-type and A-type modulations upon \mathbf{SP}_1 . Just as flipping alternate $1, 1, 1$ planes in a FM leads to the A type phase, flipping the spins in

the (111) planes alternatively in \mathbf{SP}_1 , leads to \mathbf{SP}_3 . Analogously, flipping FM lines in a FM and leads to C-type order- and a similar exercise on \mathbf{SP}_1 leads to \mathbf{SP}_2 . This modulation is also seen in the $S(\mathbf{q})$ peaks of \mathbf{SP}_2 and \mathbf{SP}_3 . See the Table I, where all the three spirals have 4 $S(\mathbf{q})$ peaks common, and \mathbf{SP}_2 and \mathbf{SP}_3 possess extra $S(\mathbf{q})$ peaks of the A-type and C-type correlations.

In scheme (ii) we take collinear phases from the phase diagram via Monte-Carlo and variational scheme (i), and compare them on very large lattices. This does not require real space diagonalisation. The simple periodicity of these phases leads to coupling between only a few $|\mathbf{k}\rangle$ states. The resulting small matrix can be diagonalized for the eigenvalues and these summed numerically. We also did it for the 'flux' phase, where the resulting matrix is a bit larger, but still it gets us access to eigenvalues for the 'flux' phase on large lattices. The details of this calculation are discussed in Appendix A. Where the collinear phases (and 'flux') seem to dominate the phase diagram we compute phase boundaries by calculating the energy on very large lattices.

III. PARTICLE-HOLE SYMMETRIC CASE

The electrons move on the cubic lattice divided into two FCC sub-lattices each of which accommodate B and B' sites. For each of these sub-lattice, one can define particle-hole transformation²⁴ for B and B' sub-lattices as $f_i \rightarrow f_i^\dagger$ and $m_{i\sigma} \rightarrow -m_{i\sigma}^\dagger$. This transforms the Hamiltonian as $H_{particle}(\Delta, t, t') - \mu N \rightarrow H_{hole}(-\Delta, t, -t') - (\mu - \Delta)N$. When $t' = 0$, this simplifies to $H(\Delta, t) - \mu N \rightarrow H(-\Delta, t) - (\mu - \Delta)N$ which reflects in the phase diagram as the repetition of the phases after half-filling. Introducing the t' hopping destroys this symmetry, but a reduced symmetry still remains relating $(\Delta, t, t') \rightarrow (-\Delta, t, -t')$, which is reflected in the phase diagrams of particle-hole asymmetric case.

We first discuss the case of particle-hole symmetry, *i.e.*, $t' = 0$, and the case of $t' \neq 0$ in the next section. For each of these cases we first discuss the MC results since these are unbiased, though affected by finite size and the cluster update mechanism. This provides a feel for the

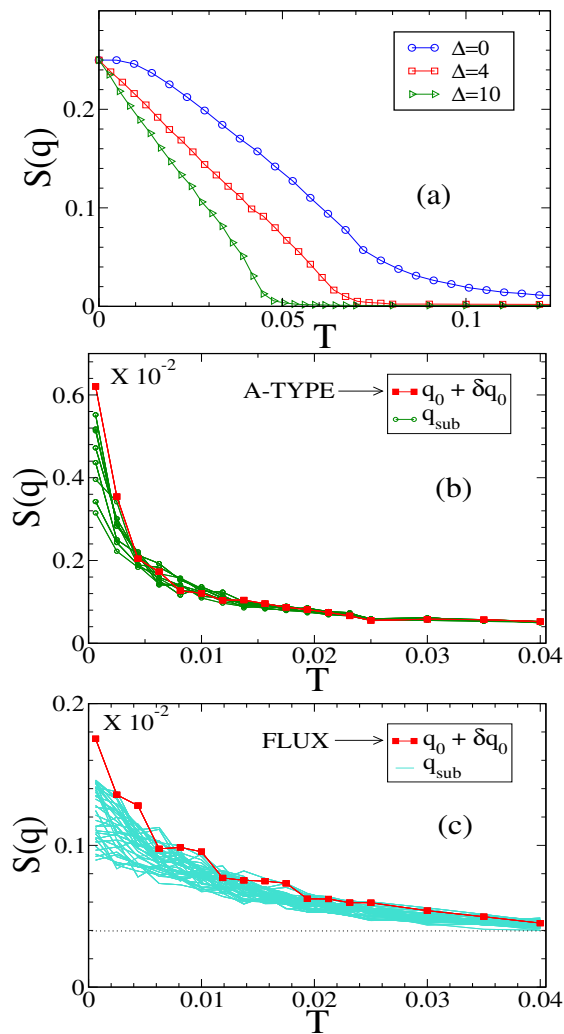


FIG. 7: Colour online: Temperature dependence of structure factor peaks for three typical densities and $t' = 0$. (a). For $\Delta = 0, 4, 10$, ferromagnetic order at $n = 0.20$. (b). The growth of A type correlations (and the noise around the principal peak, at $n = 0.50$). The ordering wave-vector \vec{q}_0 is listed in Table-I. $\delta\vec{q}_0$ are $\sim \mathcal{O}(\frac{1}{L})$ (c). ‘flux’ type correlations at $n = 1.50$. The features are at and around the ordering wave-vector in Table-I. Note the scale factors on the y axis in (b) and (c).

relevant candidate states that we can explore more carefully within a variational scheme. It also provides an estimate of T_c , not readily available within the variational scheme.

Following this we show the ground states and phase separation (PS) windows that emerge from the variational calculation for varying n and Δ/t . We also provide an alternate estimate of the “ T_c ” of these phases by calculating the energy difference $\delta E(n) = (E_{pm}(n) - E_{ord}(n))/N_s$, that the system gains via magnetic ordering. Here E_{pm} is the electronic energy averaged over disordered (paramagnetic) spin configurations while E_{ord} is the energy of the magnetically ordered ground state, both

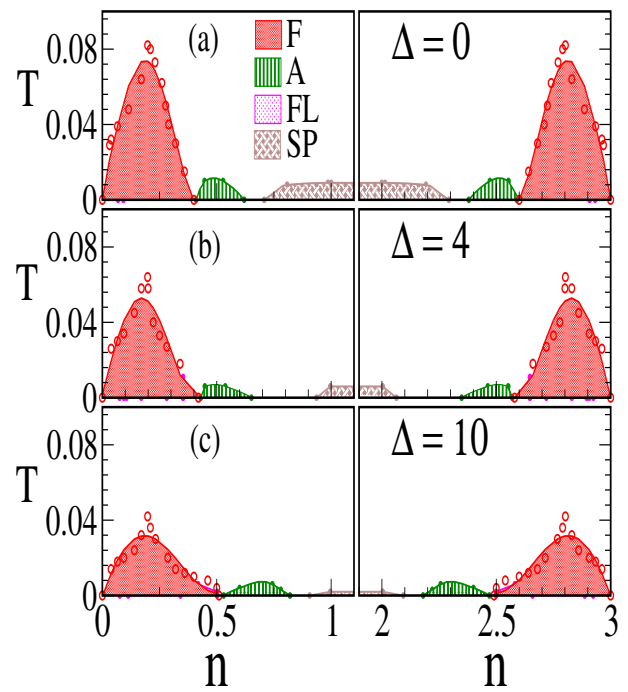


FIG. 8: Colour online: $n - T_c$ diagram for $\Delta = 0, 4, 10$ (top to bottom rows) as estimated from the Monte Carlo. Starting from low density ($n = 0$) towards high density ($n = 1$), we find FM with high T_c , thin window of A-type with very low T_c as compared to FM, followed by ‘flux’ in $\Delta = 0$ and ‘spiral’ in larger Δ case. The symbols are the actual MC estimated T_c , while the smooth lines are fit to the data.

at the same electron density n . $N_s (= \frac{N}{2})$ is the number of spins in the system. The phases that dominate the phase diagram are listed in Table-I, with the associated $\mathbf{q}_\theta, \mathbf{q}_\phi$, and the peak locations in the structure factor.

A. Monte Carlo

We studied a $N = 12^3$ system using the cluster based update scheme. We used a large but finite J to avoid explicitly projecting out any electronic states²², since that complicates the Hamiltonian matrix but allows only a small increase in system size. The magnetic phases were explored for $\Delta = 0, 4$ and 10 . An illustrative plot of peak features in $S(\mathbf{q})$ as function of temperature T , is shown in Fig.7 for some typical densities, where, for FM, $S(\mathbf{q}_{FM})$ shows monotonic decrease of T_c with increasing Δ . For A-type and ‘flux’ phase, the $S(\mathbf{q})$ data shows a number of sub-dominant \mathbf{q} peaks whose number keeps increasing as we move to more complicated phases with increasing density.

Using the structure factor data, we establish the $n - T_c$ phase diagram for $\Delta = 0, 4, 10$ that is plotted in Fig.8. The Monte Carlo captures mainly three collinear phases, namely FM, A-type, and a $\uparrow\uparrow\downarrow\downarrow$ phase. The $\uparrow\uparrow\downarrow\downarrow$ phase corresponds to two FM up planes followed by two FM

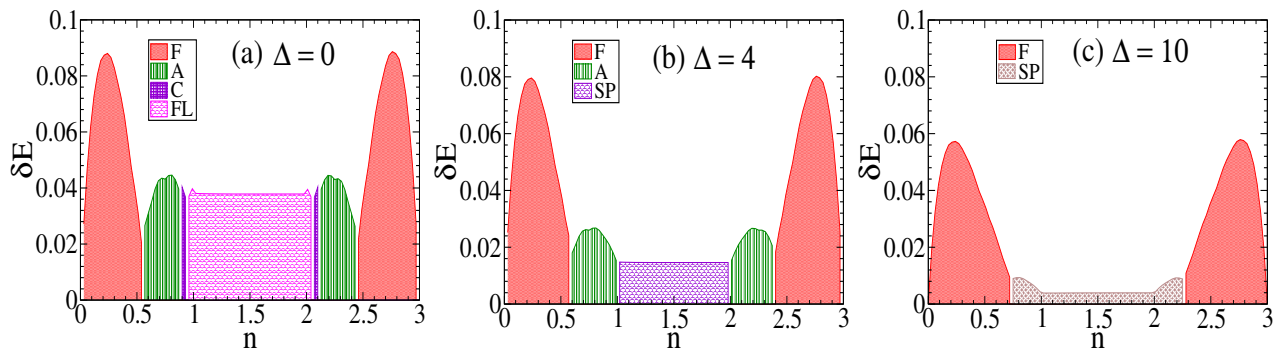


FIG. 9: Colour online: The energy difference δE of ground-state and paramagnetic phase. A variational estimate of the T_c for three values of (a) $\Delta = 0$, (b) $\Delta = 4$, (c) $\Delta = 10$ and $t' = 0$. The sequence of phases from low density to middle is FM, A, C and ‘flux’ ($\Delta = 0$) or spiral ($\Delta = 4, 10$). The decrease in the ‘ T_c ’ with Δ is more drastic in AF phases.

down planes and so forth. As the carrier density is increased via increasing μ , we find a FM phase followed by the A-type AF. A $\uparrow\downarrow\downarrow$ phase appears in a thin window surrounded by FM itself. We suspected that this as a finite size effect, and a comparison with the energy of the FM on larger lattices (20^3), shows that the FM is indeed the ground state in the thermodynamic limit, and so we consider FM and $\uparrow\downarrow\downarrow$ collectively as FM only, and presence of $\uparrow\downarrow\downarrow$ is not indicated in the phase diagram.

The FM is stable at the ends of the density window, and its region of occurrence is slowly enhanced as we increase Δ , see Fig.2 as well. The T_c however decreases with increasing Δ since the degree of B-B’ mixing (and kinetic energy) decreases.

With further increase in n the 2D system is known to make a transition to a line-like phase, and then a ‘G type’ phase (up spin surrounded by down, etc). In 3D one would expect the FM to change to a ‘planar’ (A type) phase, then a ‘line like’ (C type) phase and finally to a G type phase if possible. All of these are of course collinear phases, and geometric constraints may lead to non-collinear order as well.

While we do access the A type phase with some difficulty, our Monte Carlo cannot access the long range ordered C type phase. However, we see clear evidence of C type correlations in the structure factor. Comparing the energy of the ideal C type phase with the short range correlated phase that emerges from the MC we infer that such order is indeed preferred. However, we cannot estimate a reliable T_c scale. In the next section we will see that the variational calculation confirms the stability of the C type, among collinear phases, in this density window, and will get a rough estimate of the T_c from the energy δE .

The G type phase is geometrically disallowed on the B sub-lattice due to its FCC structure. An examination of the structure factor in the density window $n = [1, 2]$ suggests ‘flux’ like correlations at small Δ which evolves into a spiral at larger Δ . The frustration reduces the T_c of the phases in this density window compared to that

of the FM. We studied the situation in 2D, where the system is unfrustrated, and the numbers below highlight the impact of frustration. In 2D, Monte Carlo results yield $T_c^{AF}/T_c^{FM} \lesssim 1$, while in 3D $T_c^{AF}/T_c^{FM} \lesssim 0.1$. We had focused on AF states at $n \sim 1.5$. If we compare the $(\delta E)^{AF}/(\delta E)^{FM}$ for 2D and 3D, the numbers come out to be ~ 1.1 and 0.5 respectively²³. The comparisons suggest a significant decrease in the binding energy (and hence T_c) of the AF phases relative to the FM as we move from 2D to 3D.

When $t' = 0$, the electron delocalisation happens through B-B’-B paths only (see the conduction paths, for example of collinear phases A and C in Fig.4 and 5 respectively). In this case all the phases have an atomic level located at $\epsilon_{B'} (= 0)$ in the limit $J \rightarrow \infty$. This is directly seen in the density of states (DOS) of these phases. In Fig.10 we show the DOS for the F, A, C, ‘flux’ and paramagnet phases. This dispersion-less level gives constant T_c in density region $n = [1, 2]$. This feature, and several others, are modified by finite B’-B’ hopping, which leads to broadening of this level. It makes the DOS of the various magnetic phases asymmetric (in energy) and also destroys the particle-hole symmetry in the phase diagram.

B. Variational scheme

Using the approach discussed earlier, we found the ground state configurations at different electron densities. In this set we also get certain spiral phases, which are small variations of FM, A, and C phases in the left and right part of the density window. Since in these parts Monte Carlo also gives (for FM, A) clean result, we interpret it as a finite size effect. To get convinced about it, we compare the energies of these collinear phases (FM, A, C) with all their neighboring modulations $\delta \vec{q}$ s, at various lattice sizes. We find that with increasing lattice size, the per particle energy difference between collinear phase, and lowest energy candidate with the neighbor-

ing $\mathbf{q}_\theta, \mathbf{q}_\phi$, decreases, which convinces us that if we go to large enough lattice size, this difference will eventually vanish and the collinear phases (F,A,C) will be the relevant candidates.

We use a similar scheme for the middle part, however there no simple phase is suggested by this variational scheme (neither by Monte Carlo). The phases we propose for the middle density part based on this variational scheme are SP_1 , SP_2 , SP_3 , and ‘flux’. See the configurations in Fig.6 and $S(\mathbf{q})$ details from Table I.

In Fig.2, the magnetic ground state is shown for $t' = 0$ and $t' = 0.3$ (top and bottom). We see that for $t' = 0$ the phase diagram is symmetric in density. For small Δ , in the range $0 - 4$, we have FM, followed by A-type, C-type, and ‘flux’ phase. The order reverses as we go in the other half of the density window. The G-type phase which was largest stable phase in 2D (Fig.2 and Fig.5 in Ref.¹⁸) is almost taken over by the ‘flux’ phase. The stability of the ‘flux’ phase decreases with Δ and it does not show up for $\Delta > 4$.

In Fig.10, we show the DOS for F, A, C, ‘flux’ and PM phases. The upper and the lower panel correspond to $\Delta = 0$ and $\Delta = 6$ respectively. In all the phases, at all Δ , there is a spike (delta function) at $\epsilon = 0$, which accounts for the non-dispersive level at $\epsilon_{B'} = 0$.

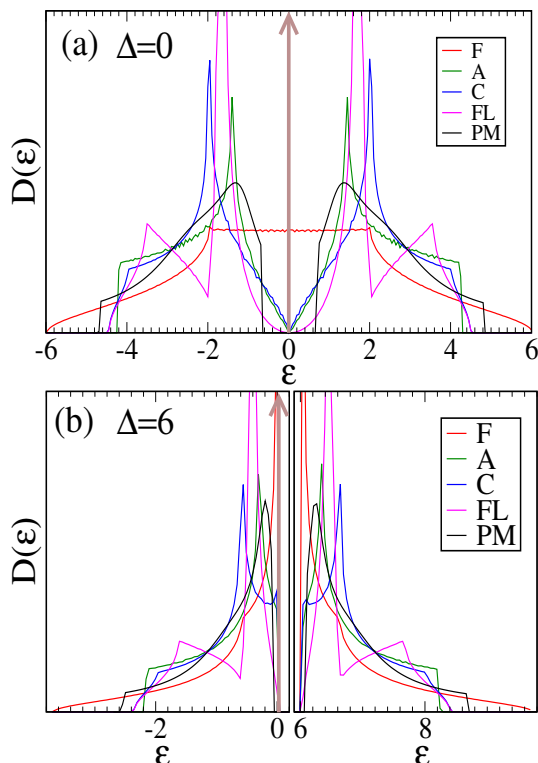


FIG. 10: Colour online: density of states for the F,A,C,FL (‘flux’) and PM (paramagnetic) phases. (a) for $\Delta = 0$ and (b) for $\Delta = 6$. In order of decreasing band width are phase F,PM,C,FL, and A (FL and C have same bandwidth). This is for both $\Delta = 0, 6$, and the order in general does not depend on the Δ

For FM all the core spins are \uparrow (say), so only \downarrow spin electrons from B’ site get to delocalise while \uparrow spin electrons remain localised at $\epsilon = 0$, which corresponds to the localised band in the spectrum and the spike in the DOS. So the localised level in FM is an \uparrow spin level. The nature of this localised level however changes when we go to AF phases. In collinear phases, its easy to understand the nature of this localised band. Take for example the case of A-type in Fig.4 down panel with conduction path. The lattice is divided into two sublattices (each of which are of layered zigzag shape), blue and red, such that, if (say) core spins in the f sites in the blue sub-lattice are all \uparrow , then the same in red sub-lattice are \downarrow . As a result, in the blue sub-lattice, \downarrow spin electrons get to delocalise, while \uparrow spin electron remain localised. the opposite happens in the red sub-lattice. Since these lattices are disconnected from each other, one can separately diagonalise them. But each of this sub-lattice, however complicated in shape, is a FM, so it gives $\frac{1}{3}$ of the levels localised at $\epsilon = 0$, which will be \uparrow spin in blue sub-lattice, while it will be \downarrow spin in red sublattice. Since both the sub-lattices have same number of sites/unit cells, we get $\frac{1}{3}$ of the levels localised at $\epsilon = 0$ but now spin degenerate. The delocalised states have also to be spin-degenerate, and their nature depends on the way the conduction paths divide the lattice into two sub-lattices.

For each spin channel the conduction paths are layered zigzag, 2 dimensional in the A type phase, while they are 3 dimensional in the C type phase.

This appearance of the localised band is not restricted to just the collinear phases, but also happens for non-collinear phases, and even the paramagnet.

IV. PARTICLE-HOLE ASYMMETRY

The model with only ‘nearest neighbour’ (BB’) hopping has a rich phase diagram. However, this has the artificial feature of a non dispersive level. In reality all materials have some degree of B’B’ hopping and we wish to illustrate the qualitative difference that results from this hopping. We explored two cases, $t' = 0.3$ and $t' = -0.3$ for these particle-hole asymmetric cases.

A. Monte Carlo

In Fig.11(a),(b) we show the structure factor data, at two densities, for (a) A type and (b) C type phases, to demonstrate one remarkable difference from the particle-hole symmetric case. As we saw earlier in Fig.7 for $t' = 0$ the structure factor data were very noisy for AF phases, with many sub-dominant \mathbf{q} peaks around the central peak. The saturation value for the A-type peak in the symmetric case was $\sim 10^{-2}$, while now it is ~ 0.2 , close to the ideal value of 0.25. The sharp change in the structure factor makes the identification of the T_c scale more reliable. Although inclusion of t' does not remove the

noise completely, it is reduced over a reasonable part of the phase diagram.

Fig.12(a) presents the $n-T_c$ phase diagram for $t' = 0.3$ and $\Delta = 0$ established from Monte Carlo, along with the δE from the variational approach (Fig.12(b)). In this case, the phases that appear as a function of density n are FM, A type, spiral, C type, A type and FM again. For FM, the window of stability gets reduced in the left (low density) part but enhanced to almost full band ($n \sim 2$ to 3) in the right (high density) part. The $\uparrow\uparrow\downarrow\downarrow$ phase appears again, but being a finite size artifact, is absorbed in the FM (and not shown). The T_c is usually reduced, from the symmetric ($t' = 0$) case, as BB' hopping provides conduction paths that are non-magnetic. There is a wider space with moderate T_c for A type phase, located asymmetrically in density. Its more stable, in the right window, than left window, hence possessing relatively higher T_c than left. The correlations of spiral and C type phases are also captured with relatively less noise, see Fig.11(b) for example of C-type correlation. Although $S(\mathbf{q})$ data for these phases still contain some noise, so that we don't get clean ground state here either. The $n-T$ phase diagram for $t' = -0.3$ and $\Delta = 0$, can be obtained from transformation $n \rightarrow 3-n$, *i.e.*, reversing the density axis of Fig.12(a),(b).

B. Variational scheme

We employ the variational scheme discussed earlier and obtain the ground state phase diagram for $t' = \pm 0.3$ is shown in Fig.13. Turning on t' has a significant effect on the phase diagram, when we use the $t' = 0$ case, Fig.2 top panel, for reference. The particle hole symmetry ($n \rightarrow 3-n$) is destroyed at finite Δ but a reduced symmetry ($n, \Delta, t' \rightarrow (3-n, -\Delta, -t')$) still holds. The phase diagram is richer in the middle of the density window where crossing among various phases occurs at different densities. Due to the symmetry mentioned above it is

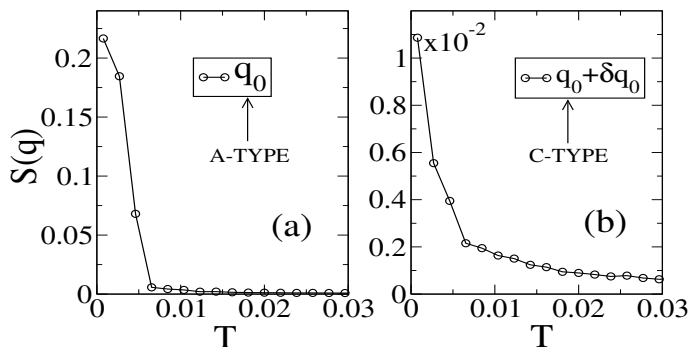


FIG. 11: $S(\mathbf{q})$ for $t' = 0.3$ and $\Delta = 0$ at (a): a typical density $n \sim 0.5$ for A-type phase and (b): a typical density $n \sim 1.2$ (this particular choice is for minimum frustration in C-type) for C type phase. A demonstration of $S(q)$ with no sub-dominant peaks, unlike at $t' = 0$.

enough to discuss the $\Delta > 0$ case with $t' = \pm 0.3$.

For $t' = 0.3$ the trends from MC are well reproduced by the variational scheme on large (20^3) systems at $\Delta = 0$. We observe reduced stability of FM at low density and enhancement at high density.

Note that the overall correspondence between the Monte Carlo and the variational approach is much better here than in the $t' = 0$ case, Fig. 8 and Fig. 9.

The A-type phase becomes very thin in the left, but unaffected by Δ , while in right side it widens up in the low Δ and gets replaced by the spiral quickly as we go up in Δ . 'flux' and C-type both become stable for high Δ with a gradual shift in the high density. For $t' = -0.3$, at very small Δ in the left and the middle part A-type and the spiral are major candidates with small window for C-AF and 'flux'. The behaviour in this part is not very sensitive to sign of t' .

Focusing on $t' = -0.3$, as go up from $\Delta = 0$ to $\Delta \sim 5$ the AF phases become less and less stable and are almost wiped out from the left part of the density, and FM becomes stable there. The largest stability window of FM occurs roughly near $\Delta \sim 5$, where its stable upto $n \sim 1.8$. Going further with higher Δ , FM loses its stability, from C type, 'flux' and spirals. However, there is very thin strip of stability of the FM in the band edge in the left part, and towards the middle density, there is re-entrance of the FM phase.

In the right part of the density, we have FM, A type and spiral. Increasing Δ reduces the stability of A type to FM, making it vanish near $\Delta \sim 7$, while FM window

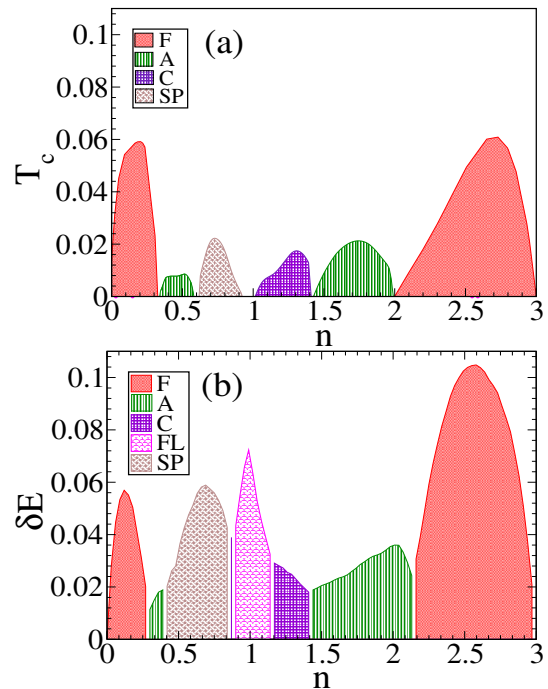


FIG. 12: Colour online: Phase diagram obtained via Monte Carlo (top) and from the variational calculation (bottom) at $t' = 0.3$ and $\Delta = 0$.

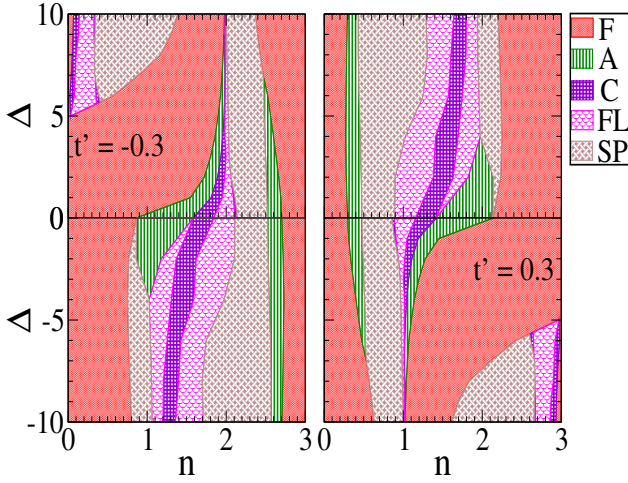


FIG. 13: Colour online: Ground state phase diagram in the presence of t' . Left panel: $t' = -0.3$. Right panel: $t' = 0.3$.

keeps increasing with Δ .

The DOS for the ordered F, A, C, ‘flux’ phase and the paramagnet are shown in Fig.14. (a) For $t' = 0.3$, $\Delta = 0$ FM has the largest bandwidth, with paramagnet second largest. The band edges of A, C, ‘flux’ almost coincide both for small and large Δ . (b) For $t' = 0.3$, $\Delta = 6$ the left band shows that all the phases seem to have ‘almost’ similar features in the DOS, while the right band shows distinct features of each of the phases, similar to $t' = 0$ DOS. (c) For $t' = -0.3$, $\Delta = 6$ however, has a distinct case. Here the lower edge of the band for FM, ‘flux’ and C coincide, and the DOS of ‘flux’, or C, is higher than FM, which explains why FM becomes unstable in the left side and taken by ‘flux’ and C, upon increasing Δ .

We also estimate the phase separation boundaries between FM, A, C phases shown in Fig.15. For $t' = 0$ and for $\Delta > 0$, we see that PS regions are significant, while they vanish for $\Delta < 0$ as we go down. For $t' = 0.3$, (right panel) the PS boundaries are too narrow to be visible.

In Fig.16 we have shown the $\delta E(n)$ calculated for 20^3 size, for $\Delta = 4$, $t' = -0.3$, with the large stability window of ferromagnet (See Fig.12). Here, though the Δ and t' are non-zero, due to unusually large stability window, the δE (or T_c) is large.

To summarise, from the MC and variational data we learn that, apart from asymmetry in the phase diagram, collinear FM and A type phases become stable in wide density window. Their T_c however is slightly reduced than the symmetric case. The $S(\mathbf{q})$ data showing less noise for A, C type and spirals indicates that the energy landscape become ‘smoother’ by t' so that annealing process becomes easier to get to the ground state. The energy differences δE as well as MC estimated T_c s show overall decrease with t' . This is understandable as, by introducing t' we allow electrons to move on the ‘non-magnetic’ sub-lattice B'. Now the energy of any phase, depends on the energy gain via the hopping process. From the nearest $f - m$ hopping, this gain scales as $\frac{t^2}{\Delta}$

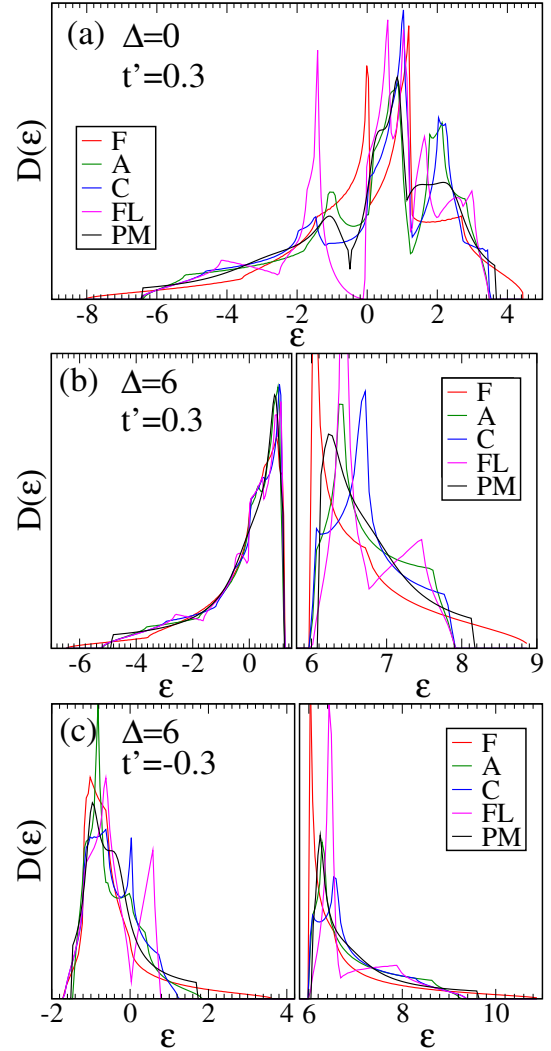


FIG. 14: Colour online: DOS for the F, A, C, FL, PM phases (a): $\Delta = 0$, $t' = 0.3$, there is no resemblance to the particle-hole symmetric case. FM and PM have largest bandwidth, while A, C, ‘flux’ have almost same bandwidth (b): $\Delta = 6$, $t' = 0.3$, due to large band-gap, two bands are shown in two different panels (left, right) the same bandwidth order, right band less effected from t' , being situated around Δ (c): $\Delta = 6$, $t' = -0.3$. The structure of the band edges has changed drastically. Now band edges of the FM, ‘flux’ and C type coincide on the left, while on the right edge of the first panel FM is more widespread.

subject to spin configurations, while the from the next nearest $m - m$ hopping, this gain simply scales as t' , and doesn’t care upon spin configurations. So more we increase t' and Δ , the more we are making the energy of the system insensitive to spin-configurations. The asymptotic limit of this is $\frac{t^2}{\Delta} \rightarrow 0$ when every phase has same energy as paramagnet. That also explains why the phase separation windows become very small with inclusion of t' .

In the couple of paragraphs below we try to create an understanding of how the phase diagram is affected by

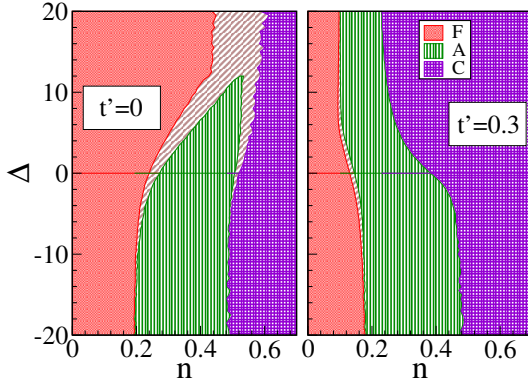


FIG. 15: Colour online: PS regions. left column for $t'=0$ and right column of $t'=0.3$. Notice that PS regions are significant for $\Delta > 0$ and $t' = 0$, for $t' \neq 0$ and for $\Delta < 0$ PS boundaries almost vanish.

t' . There isn't, unfortunately, an understanding of the effects over the entire density window, but we can at least motivate the changes at low density.

For $t' = -0.3$, the FM loses its stability to AF phases even at low n . That is puzzling since one would expect the FM phase to have the largest bandwidth. We recall that in the $t' = 0$ case, there is a localised band coming from B' level for all the phases. The dispersion of this previously localised level causes the m and f to have a \mathbf{k} dependent separation, which was Δ for all \mathbf{k} in the symmetric case. The separation for these levels in the asymmetric case is $\Delta_{\mathbf{k}} = \Delta - \epsilon'_{\mathbf{k}}$, which varies from $\Delta - 12|t'|$, to $\Delta + 12|t'|$ in 3D. In 2D it varies from from $\Delta - 4|t'|$, to $\Delta + 4|t'|$.

If we consider the simpler 2D case for illustration, $\epsilon'_{\mathbf{k}} = -4t' \cos k_1 \cos k_2$, which, for $t' > 0$ is minimum at $\mathbf{k}=(0,0), (\pi, \pi)$ while the maximum is at $\mathbf{k}=(\pi, 0), (0, \pi)$. For $t' < 0$ the opposite will happen. Thus, for $t' > 0$ $\mathbf{k}=(0,0), (\pi, \pi)$ and neighbouring states will experience enhanced mixing $\sim \Delta - 4|t'|$, while, the states near $\mathbf{k}=(\pi, 0), (0, \pi)$ experience lower mixing. In the ferro-

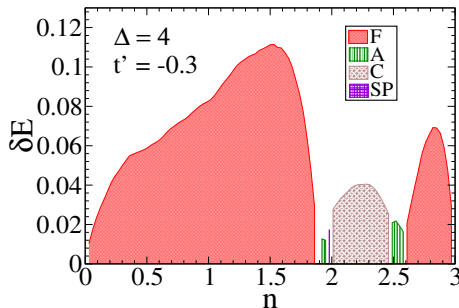


FIG. 16: Colour online: Asymmetric case, the energy difference δE of ground-state and paramagnetic phase. Top: $\Delta = 4, t' = -0.3$ where FM is stable in the large portion of the density. Bottom: $\Delta = 0, t' = 0.3$ The trends of δE match with T_c .

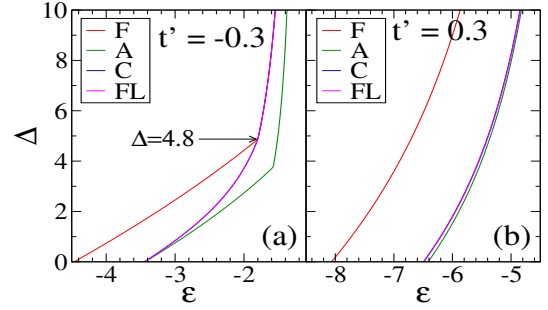


FIG. 17: Colour online: Asymmetric case, lowest eigenvalues plotted as function of Δ for the F,A,C and flux phases calculated from the dispersions. (a) $t' = -0.3$ and (b) $t' = 0.3$

magnet (both in 2D and 3D), the lowest eigenvalue corresponds to $\mathbf{k} = (0, 0)$, while (for 2D) the G-type phase has lowest eigenvalues at $\mathbf{k} = (0, 0), (\pi, 0), (0, \pi), (\pi, \pi)$. Therefore, for $t' < 0$, the lowest eigenvalues of both the phases are enhanced but the band-edge of FM stays lower than G type. While in the other, the strongest mixing states are $(\pi, 0)$ and $(0, \pi)$, which aren't at the edge for FM, its band-edge gets lower enhancement, while the band-edge of G type gets lowered. For a given t' , as we increase Δ , a point comes where band edges of the FM and G, coincide. This is the point where FM loses its stability.

The same argument can be extended to 3D, with C and flux phases, just the role of the qs gets extended to 3D (e.g. $(\pi, 0, 0)$ etc), and the correction in the separation is $\sim 12t'$ instead of $\sim 4t'$. In Fig. 17 we have shown the plot of lowest eigenvalues of F,A,C and flux phases with Δ for $t' = \pm 0.3$

Finally, a comment (mainly a conjecture), Fig.18, on how the energy landscape of the DP model changes on addition of t' . We already know that the 'binding energy' and T_c of magnetic phases reduce with increasing t' - but also that the 'noise' in the cooling process also reduces quickly.

If $t' \gg t$ then the electrons could delocalise on the wide t' based band populating the non magnetic sites only. Magnetic order would make little difference to electronic energies and the 'energy landscape' in the space of spin configurations would be featureless, panel (c) in Fig.18. There are no global minima, *i.e.* ordered states, and no local minima either. If $t' = 0$ then delocalisation takes place necessarily through the magnetic sites and the deep minima in configuration space represent ordered states while the 'grassy' features indicate shallow metastable states close to them. Our MC data probing AF states at $t' = 0$ suggests this picture, curve (a) in Fig.18. At intermediate t' the ordered states are shallower, but the metastable states seem to have been affected even more drastically, if our MC data, Fig.11, is to be taken seriously.

While the discussion above seems to be merely an analysis of trends in the MC annealing process, a simpler energy landscape would make the occurrence of AF states

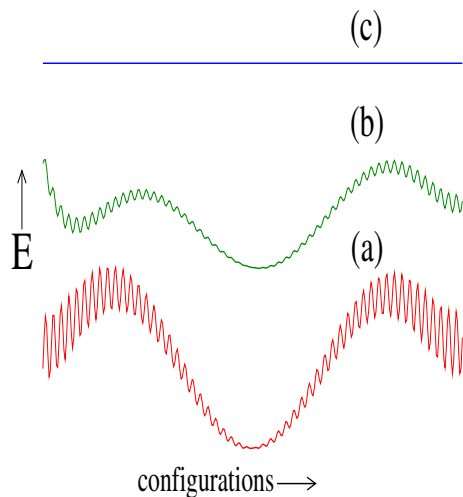


FIG. 18: Colour online: A schematic energy landscape of the double perovskite model, in the space of spin configurations, for (a). $t'/t = 0$, (b). $t'/t \sim \mathcal{O}(1)$, and (c). $t'/t \rightarrow \infty$. The panels are indicated for a fixed set of electronic parameters, except t' which varies as indicated above. At $t' = 0$ the landscape has many local minima around the deep minimum, and while the ‘binding energy’ of the ordered state, with respect to the paramagnet, is large (and so also the T_c) the system is apt to get stuck in one of the neighbouring minima in the cooling process. When $t'/t \rightarrow \infty$ magnetic order makes no difference to the energy, the electrons bypass the magnetic sites. At intermediate t' , while the binding energy and T_c are smaller, the local minima also seem to be fewer and shallower. This makes the ordered state easier to access.

more likely in the real materials as well.

V. DISCUSSION

The real double perovskites are multiband materials, involving additional interaction effects and antisite disorder beyond what we have considered in this paper. We feel it is necessary to understand in detail the phase diagram of the ‘simple’ model we have studied, and then move to more realistic situations. Below, we first provide a qualitative comparison of the trends we observe with experimental data, and then move to a discussion of additional interactions.

There are no clear experimental signatures of metallic AF phases yet, driven by the kind of mechanism that we have discussed. So, the comparison to experiments is, at the moment, confined to the T_c scales^{25,26} *etc.*, of the ferromagnetic DP’s. In a material like SFMO the electron density can be increased by doping La for Sr, *i.e.*, compositions like $\text{Sr}_{2-x}\text{La}_x\text{FeMoO}_6$. This was tried²⁵ and the T_c increased from 420K at $x = 0$ to $\sim 490\text{K}$ at $x = 1$. SFMO has threefold degeneracy of the active, t_{2g} , orbitals while we have considered a one band model. When we create a correspondence by dividing the electron count by the maximum possible per unit cell (3 in our case, 9

in the real material), in our units $x = 0$ corresponds to $n = 0.33$ and $x = 1$ to $n = 0.66$.

When $t' = 0$, as a function of n the T_c peaks around $n = 0.2$, Fig.8, quite far from the experimental value. However, in the presence of $t' = -0.3$ and $\Delta = 4$, Fig.16, the peak occurs above $n = 1$. So, modest t' can generate the ferromagnetic window that is observed, and produce a $T_c \sim 0.1t$. For $t = 0.5\text{eV}$, this is in the right ballpark.

Unfortunately, attempts to increase n via A site substitution also brings in greater antisite disorder (B-B’ interchange) and even the possibility of newer patterns of A site ordering (!) complicating the analysis. For example, one would try compositions of the form: $\text{A}_{2-x}\text{A}'_x\text{BB}'\text{O}_6$, where A and A’ have different valence in an attempt to change n . The assumption is that the A’ only changes n without affecting other electronic parameters, *i.e.*, A’ ions do not order and remain in an alloy pattern. This may not be true. In fact, at $x = 1$, the material $\text{AA}'\text{BB}'\text{O}_6$ may have a specific A-A’-B-B’ ordering pattern that affects electronic parameters in a non trivial way and one cannot understand this material as a perturbation on $\text{A}_2\text{BB}'\text{O}_6$. In such a situation one needs guidance from experiments and *ab initio* theory to fix electronic parameters as x is varied. All this before one even considers the inevitable antisite (B-B’) disorder and its impact on magnetism? .

VI. CONCLUSIONS

We have studied a one band model of double perovskites in three dimensions in the limit of strong electron-spin coupling on the magnetic site. The magnetic lattice in the cubic double perovskites is FCC and increasing the electron density leads from the ferromagnet, through A and C type collinear antiferromagnets, to spiral or ‘flux’ phases close to half-filling. We estimate the T_c of these phases, via Monte Carlo and variational calculation, and find the AF T_c to be significantly suppressed compared to the 2D case. We attribute it to the geometric frustration on the FCC lattice. The introduction of B’B’ hopping $t'/t \sim 0.3$ significantly alters the phase diagram and T_c scales and creates a closer correspondence to the experimental situation on DP ferromagnets.

Acknowledgments

We acknowledge use of the high performance computing facility at HRI. PM was supported by a DAE-SRC Outstanding Research Investigator Award, and the DST India via the Indo-EU ATHENA project.

Appendix A

Here we show how to calculate dispersion for selected ordered phases, which have relatively small unit cells. We define the unit cell for each phase, and go to k -space where the hamiltonian becomes block diagonal.

1. Spectrum for collinear phases

The Hamiltonian can be diagonalized by Fourier transformation We write the Hamiltonian H as $H = H_0 + H_J$, where, H_0 is given by,

$$H_0 = \sum_{\vec{X},\sigma} [\epsilon_1 f_{\vec{X},\sigma}^\dagger f_{\vec{X},\sigma} + \epsilon_2 m_{\vec{X}+\vec{a}_1,\sigma}^\dagger m_{\vec{X}+\vec{a}_1,\sigma}^\dagger] - t' \sum_{\vec{X},\sigma} \sum_{\vec{\delta} \in \text{NNN}} (m_{\vec{X}+\vec{a}_1,\sigma}^\dagger m_{\vec{X}+\vec{a}_1+\vec{\delta},\sigma} + \text{h.c.}) - t \sum_{\vec{X},\sigma} \sum_{\vec{\delta} \in \text{NN}} (f_{\vec{X},\sigma}^\dagger m_{\vec{X}+\vec{\delta},\sigma} + \text{h.c.}) \quad (\text{A1})$$

and H_J is given by

$$H_J = J \sum_{\vec{X}} \vec{S}(\vec{X}) \cdot \vec{\sigma}_{\alpha,\beta} f_{\vec{X},\alpha}^\dagger f_{\vec{X},\beta} \quad (\text{A2})$$

The lattice vector \vec{X} is defined as $\vec{X} = n_1 \vec{A}_1 + n_2 \vec{A}_2 + n_3 \vec{A}_3$ with $A_i, i = 1, 2, 3$ as the primitive lattice vectors ($A_1 = (2, 0, 0)$, $A_2 = (1, 1, 0)$, $A_3 = (0, 1, 1)$), defining the periodicity of lattice with the 2 site unit cell. With this periodicity, the unit cell has one "f" and one "m" site at $(0, 0, 0)$ and $(1, 0, 0)$ respectively. Now doing a Fourier transform on "f" operators (similarly for "m"s)

$$f_{\vec{X},\sigma}^\dagger = \frac{1}{\sqrt{N}} \sum_{\vec{k}} f_{\vec{k},\sigma}^\dagger \exp(i\vec{k} \cdot \vec{X}) \quad (\text{A3})$$

$$f_{\vec{X},\sigma} = \frac{1}{\sqrt{N}} \sum_{\vec{k}} f_{\vec{k},\sigma} \exp(-i\vec{k} \cdot \vec{X}) \quad (\text{A4})$$

This simplifies the non-magnetic part H_0 as follows,

$$H_0 = \sum_{\vec{k},\sigma} [(\epsilon_2 + A'_k) m_{\vec{k},\sigma}^\dagger m_{\vec{k},\sigma} + \epsilon_1 f_{\vec{k},\sigma}^\dagger f_{\vec{k},\sigma} + (A_{\vec{k}} f_{\vec{k},\sigma}^\dagger m_{\vec{k},\sigma} + \text{h.c.})] \quad (\text{A5})$$

$$= \sum_{\vec{k},\sigma} \begin{pmatrix} f_{\vec{k},\sigma}^\dagger & m_{\vec{k},\sigma}^\dagger \end{pmatrix} \begin{pmatrix} \epsilon_1 & A_{\vec{k}} \\ A_{\vec{k}} & \epsilon_2 + A'_k \end{pmatrix} \begin{pmatrix} f_{\vec{k},\sigma} \\ m_{\vec{k},\sigma} \end{pmatrix} \quad (\text{A6})$$

Which is reduced to 2×2 block. the amplitudes $A_{\vec{k}}$ and A'_k are just the cubic and FCC dispersions given by

$$A_{\vec{k}} = -2t(\cos k_x + \cos k_y + \cos k_z) \quad \text{and} \\ A'_k = -4t'(\cos k_x \cos k_y + \cos k_y \cos k_z + \cos k_z \cos k_x)$$

Next, we have to simplify the H_J part. For the collinear phases, $\vec{S}(\vec{X})$ can be expressed as

$$\vec{S}(\vec{X}) = \begin{pmatrix} 0 \\ 0 \\ 1 \end{pmatrix} \exp(i\vec{q} \cdot \vec{X}) \quad (\text{A7})$$

For FM, \vec{q} is trivially $(0, 0, 0)$. For A-type, $\vec{q} = (\frac{\pi}{2}, -\frac{\pi}{2}, \frac{\pi}{2})$, while for C-type $\vec{q} = (0, \pi, -\pi)$. Now, plugging this value of $\vec{S}(\vec{X})$ in H_J and doing the Fourier transform for the H_J , we get,

$$H_J = J \sum_{\vec{x}} \sigma f_{\vec{k},\sigma}^\dagger f_{\vec{k}+\vec{q},\sigma} \quad ; \sigma = \pm 1 \quad (\text{A8})$$

Now $\vec{q} = 0$ for FM, so H_J becomes diagonal. Thus total hamiltonian H still remains 2×2 block, and the eigenvalues for the FM are solutions of the following 2×2 block

$$H_{2 \times 2}(\vec{k}, \sigma) = \begin{pmatrix} \epsilon_1 + J\sigma & A_{\vec{k}} \\ A_{\vec{k}} & \epsilon_2 + A'_k \end{pmatrix} \quad (\text{A9})$$

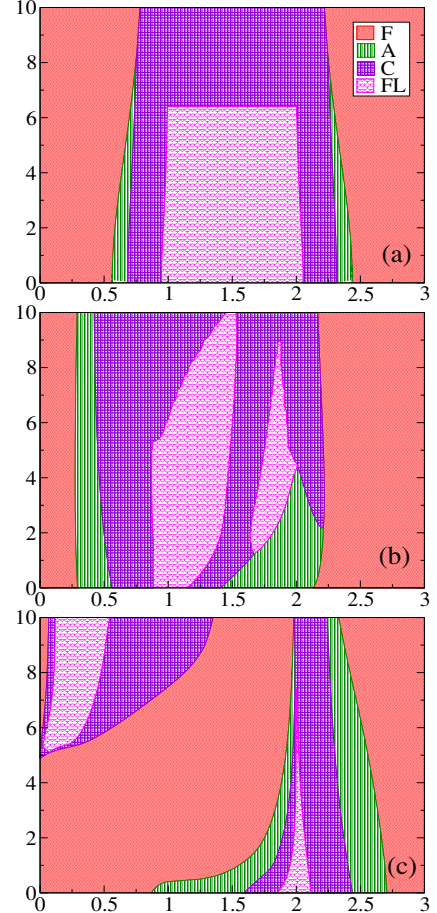


FIG. 19: Colour online: Phase diagram based on k space based diagonalisation for $t' = 0, 0.3, -0.3$. System size $N = 160^3$. Here we can only use F, A, C and 'flux' phase as candidate states but some of the complexity of more elaborate phase diagrams, Fig.2, are already present.

For A-type and C-type phases, we get matrix elements connecting $|\vec{k}, \sigma\rangle \rightarrow |\vec{k} + \vec{q}, \sigma\rangle \rightarrow |\vec{k}, \sigma\rangle$, so that now we get to solve following 4×4 block

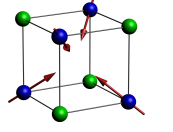
$$H_{4 \times 4}(\vec{k}, \sigma) = \begin{pmatrix} \epsilon_1 & J\sigma & A_{\vec{k}} & 0 \\ J\sigma & \epsilon_1 & 0 & A_{\vec{k}+\vec{q}} \\ A_{\vec{k}} & 0 & \epsilon_2 + A'_{\vec{k}} & 0 \\ 0 & A_{\vec{k}+\vec{q}} & 0 & \epsilon_2 + A'_{\vec{k}} \end{pmatrix} \quad (\text{A10})$$

From these we obtain the spectrum for F,A,C phases on large ($\sim 100^3 - 500^3$) lattices, which can be used to calculate the density of states, phase diagram, phase separation windows etc.

2. Spectrum for the ‘flux’ phase

The unit cell for the ‘flux’ phase has $4B$, and $4B'$ atoms lying on the corners of the cube.

The primitive lattice vectors become $A_i = \{(2, 0, 0), (0, 2, 0), (0, 0, 2)\}$. At finite J , the same procedure (as for collinear phases) will reduce the hamiltonian into 16×16 block. To make life a bit simple, we use the $J \rightarrow \infty$ limit on the hamiltonian for the ‘flux’ phase, which is same as used in¹⁸ except its the 3D version.



This gives us 4 spinless f_i levels and 8 $m_{i,\sigma}$ levels in the unit cell, which upon simplification reduces to 12×12 block. With the basis $(f_i(k) m_{i\uparrow}(k))_{i \in \{1,2,3,4\}}$ The hamiltonian breaks into 12×12 block given as follows

$$H = \begin{pmatrix} \Delta & 0 & 0 & 0 & t_{1\uparrow}a_1 & t_{1\downarrow}a_1 & t_{1\uparrow}a_2 & t_{1\downarrow}a_2 & 0 & 0 & t_{1\uparrow}a_3 & t_{1\downarrow}a_3 \\ 0 & \Delta & 0 & 0 & t_{2\uparrow}a_2 & t_{2\downarrow}a_2 & t_{2\uparrow}a_1 & t_{2\downarrow}a_1 & t_{2\uparrow}a_3 & t_{2\downarrow}a_3 & 0 & 0 \\ 0 & 0 & \Delta & 0 & t_{3\uparrow}a_3 & t_{3\downarrow}a_3 & 0 & 0 & t_{3\uparrow}a_2 & t_{3\downarrow}a_2 & t_{3\uparrow}a_1 & t_{3\downarrow}a_1 \\ 0 & 0 & 0 & \Delta & 0 & 0 & t_{4\uparrow}a_3 & t_{4\downarrow}a_3 & t_{4\uparrow}a_1 & t_{4\downarrow}a_1 & t_{4\uparrow}a_2 & t_{4\downarrow}a_2 \\ t_{1\uparrow}^*a_1 & t_{2\uparrow}^*a_2 & t_{3\uparrow}^*a_3 & 0 & 0 & 0 & t_{12} & 0 & t_{23} & 0 & t_{13} & 0 \\ t_{1\downarrow}^*a_1 & t_{2\downarrow}^*a_2 & t_{3\downarrow}^*a_3 & 0 & 0 & 0 & 0 & t_{12} & 0 & t_{23} & 0 & t_{13} \\ t_{1\uparrow}^*a_2 & t_{2\uparrow}^*a_1 & 0 & t_{4\uparrow}^*a_3 & t_{12} & 0 & 0 & 0 & t_{13} & 0 & t_{23} & 0 \\ t_{1\downarrow}^*a_2 & t_{2\downarrow}^*a_1 & 0 & t_{4\downarrow}^*a_3 & 0 & t_{12} & 0 & 0 & 0 & t_{13} & 0 & t_{23} \\ 0 & t_{2\uparrow}^*a_3 & t_{3\uparrow}^*a_2 & t_{4\uparrow}^*a_1 & t_{23} & 0 & t_{13} & 0 & 0 & 0 & t_{12} & 0 \\ 0 & t_{2\downarrow}^*a_3 & t_{3\downarrow}^*a_2 & t_{4\downarrow}^*a_1 & 0 & t_{23} & 0 & t_{13} & 0 & 0 & 0 & t_{12} \\ t_{1\uparrow}^*a_3 & 0 & t_{3\uparrow}^*a_1 & t_{4\uparrow}^*a_2 & t_{13} & 0 & t_{23} & 0 & t_{12} & 0 & 0 & 0 \\ t_{1\downarrow}^*a_3 & 0 & t_{3\downarrow}^*a_1 & t_{4\downarrow}^*a_2 & 0 & t_{13} & 0 & t_{23} & 0 & t_{12} & 0 & 0 \end{pmatrix}$$

Where the symbols in the above are defined as $\alpha = \sqrt{\frac{\sqrt{3}+1}{2\sqrt{3}}}$; $\beta = \sqrt{\frac{\sqrt{3}-1}{2\sqrt{3}}}$; $z = \frac{1-i}{\sqrt{2}}$

$$a_1 = 2 \cos k_1; \quad a_2 = 2 \cos k_2; \quad a_3 = 2 \cos k_3; \quad t_{12} = -4t' \cos k_1 \cos k_2; \quad t_{23} = -4t' \cos k_2 \cos k_3; \\ t_{13} = -4t' \cos k_1 \cos k_3; \quad t_{1\uparrow} = t_{2\uparrow} = -t\alpha; \quad t_{3\uparrow} = t_{4\uparrow} = -t\beta; \quad t_{1\downarrow} = -t_{2\downarrow} = tz\beta; \quad t_{3\downarrow} = -t_{4\downarrow} = -tz^*\alpha$$

¹ For reviews, see D. D. Sarma, Current Op. Solid St. Mat. Sci.,**5**, 261 (2001), D. Serrate, J. M. de Teresa and M. R. Ibarra, J. Phys. Cond. Matt. **19**, 023201 (2007).

² Mark T. Anderson, Kevin B. Greenwood, Gregg A. Taylor, and Kenneth R. Poeppelmeier. Progress in Solid State Chemistry, **22**, 197 (1993).

³ K.-I. Kobayashi, T. Kimura, H. Sawada, K. Terakura, and Y. Tokura. Nature (London) **395**, 677, (1998).

⁴ M.A. Subramanian N.S. Rogado, J. Li. Advances in Materials **17**, 2225 (2005).

⁵ Hena Das, Umesh V. Waghmare, T. Saha-Dasgupta, and D. D. Sarma. Phys. Rev. Lett. **100**, 186402, (2008).

⁶ Hena Das, Molly De Raychaudhury, and T. Saha-Dasgupta. Appl. Phys. Lett. **92**, 201912 (2008).

⁷ D. D. Sarma, Priya Mahadevan, T. Saha-Dasgupta, Sugata Ray, and Ashwani Kumar. Phys. Rev. Lett. **85**, 2549 (2000).

⁸ J. B. Philipp, P. Majewski, L. Alff, A. Erb, R. Gross, T. Graf, M. S. Brandt, J. Simon, T. Walther, W. Mader, D. Topwal, and D. D. Sarma. Phys. Rev. B **68**, 144431

- (2003).
- ⁹ P. Majewski, S. Geprägs, A. Boger, M. Opel, A. Erb, R. Gross, G. Vaitheeswaran, V. Kanchana, A. Delin, F. Wilhelm, A. Rogalev, and L. Alf. *Phys. Rev. B* **72**, 132402 (2005).
 - ¹⁰ Y. Krockenberger, K. Mogare, M. Reehuis, M. Tovar, M. Jansen, G. Vaitheeswaran, V. Kanchana, F. Bultmark, A. Delin, F. Wilhelm, A. Rogalev, A. Winkler, and L. Alf. *Phys. Rev. B* **75**, 020404 (2007).
 - ¹¹ Tapas Kumar Mandal, Claudia Felser, Martha Greenblatt, and Jürgen Kübler. *Phys. Rev. B* **78**, 134431 (2008).
 - ¹² A. Chattopadhyay and A. J. Millis. *Phys. Rev. B* **64**, 024424 (2001).
 - ¹³ K. Phillips, A. Chattopadhyay, and A. J. Millis. *Phys. Rev. B* **67**, 125119 (2003).
 - ¹⁴ M. Hamada and H. Shimahara. *Phys. Rev. B* **51**, 3027 (1995).
 - ¹⁵ D. F. Agterberg and S. Yunoki. *Phys. Rev. B* **62**, 13816 (2000).
 - ¹⁶ J. L. Alonso, J. A. Capitán, L. A. Fernández, F. Guinea, and V. Martín-Mayor. *Phys. Rev. B* **64**, 054408 (2001).
 - ¹⁷ K. Pradhan and P. Majumdar, *Europhys. Lett.* **85**, 37007 (2009).
 - ¹⁸ Prabuddha Sanyal and Pinaki Majumdar. *Phys. Rev. B* **80**, 054411 (2009).
 - ¹⁹ Sanjeev Kumar and Pinaki Majumdar. *EPJ B* **50**, 571 (2006).
 - ²⁰ Prabuddha Sanyal, Hena Das, and T. Saha-Dasgupta. *Phys. Rev. B* **80**, 224412 (2009).
 - ²¹ Shuai Dong, Rong Yu, Seiji Yunoki, J.-M. Liu, and Elbio Dagotto. *Phys. Rev. B* **78**, 155121 (2008).
 - ²² We have worked on $\Delta \in [-10, 10]$, so J has to be large compared to it. We used $J = 1000$, as the atomic bands which, for finite J , are actually dispersive (of band-width $\sim \mathcal{O}(\frac{1}{\Delta})$) become actually atomic to required numerical accuracy.
 - ²³ We compared ratio of the maximum of $(\delta E)^{FM}$ and maximum of $(\delta E)^{AF}$ in the density window, for $\Delta = 0$ and $t' = 0$
 - ²⁴ Patrik Fazekas, *Lecture Notes on Electron Correlation and Magnetism*, Chapter 4.5, World Scientific.
 - ²⁵ J. Navarro, C. Frontera, L. Balcells, B. Martinez, and J. Fontcuberta, *Phys. Rev. B* **64**, 092411 (2001).
 - ²⁶ B.-G. Park, Y.-H. Jeong, and J.-H. Park, J. H. Song, J.-Y. Kim, H.-J. Noh, H.-J. Lin and C. T. Chen, *Phys. Rev. B* **79**, 035105 (2009).
 - ²⁷ Viveka Nand Singh and Pinaki Majumdar, arXiv:1009.1709.